Optical phonon dominated heat transport: A first-principles thermal conductivity study of math xmlns="http://www.w3.org/1998/Math/MathML">msub>mi>BaSnS/mi>mn>2/mn>/msub>/math>

Zhi Li, Hongyao Xie, Shiqiang Hao, Yi Xia, Xianli Su, Mercouri G. Kanatzidis, Christopher Wolverton, and Xinfeng Tang

Phys. Rev. B **104**, 245209 — Published 23 December 2021
DOI: 10.1103/PhysRevB.104.245209

Optical phonon dominated heat transport: a first-principles thermal conductivity study of $BaSnS_2$

Zhi Li,[†,‡] Hongyao Xie,[*,‡] Shiqiang Hao,[§] Yi Xia,[§] Xianli Su,[†] Mercouri G. Kanatzidis,[*,‡] Christopher Wolverton,[*,§] Xinfeng Tang[*,†]

[†] State Key Laboratory of Advanced Technology for Materials Synthesis and Processing, Wuhan University of Technology, Wuhan 430070, China

[‡] Department of Chemistry, Northwestern University, Evanston, Illinois 60201, United States

[§] Department of Materials Science and Engineering, Northwestern University, Evanston, Illinois 60208, United States

Abstract

Acoustic phonons with long mean free paths have long been believed to control the lattice thermal conductivity κ_L in solids dominantly. In this study, however, we demonstrate an optical-phonon-dominated κ_L in $BaSnS_2$. By solving Peierls–Boltzmann transport equation (PBTE), we predict a low diagonal lattice thermal conductivity κ_L(D) of 0.34 W m^{-1} K^{-1} at 850 K, which is less than half the κ_L(D) of SnS at the same temperature. Further calculations following Allen–Feldman model suggest the additional off-diagonal lattice thermal conductivity κ_L(OD) contributed by wave-like tunneling phonons. The κ_L(OD) becomes pronounced at the high temperature (0.17 W m^{-1} K^{-1} at 850 K) and leads to a deviation of the temperature dependence of κ_L from T^{-1} to $T^{-0.76}$, suggesting the potential lattice anharmonicity in $BaSnS_2$. Further analyses indicate $BaSnS_2$ has over 68% of κ_L contributed by optical phonons. We show this uncommon optical-phonon-dominated κ_L is due to the relatively high group velocities of optical phonons in $BaSnS_2$. The phonon mode visualization suggests these relatively high-velocity optical phonons correspond to the anti-phase vibrations in $BaSnS_2$ monolayers, which is originated from the unique permutation of SnS_3 tetrahedrons. Finally, by investigating the mode-resolved group velocity, relaxation time, and Grüneisen parameter, we attribute the intrinsic low κ_L of $BaSnS_2$ to the soft lattice and the relatively high lattice anharmonicity induced by the Ba–S weak bonding and Sn(II) lone pair electrons. Our study explicitly analyzes the microscopic mechanism of optical-phonon-dominated heat transport in $BaSnS_2$ and suggests it worthy of further experimental studies as an intrinsic-low-κ_L material.

Keywords: thermal conductivity, wave-like tunneling phonons, optical phonons, group velocity, lattice anharmonicity

I. INTRODUCTION

Materials with low lattice thermal conductivity κ_L have received much attention in many science and technology fields, including thermoelectricity [1,2], heat management [3,4], and thermal barrier coatings [5]. To search for these materials, we must first understand the underlying heat transport mechanism. In crystals, heat is transported, in part, by the propagation of vibration modes. The phonon gas model has been widely used to describe such particle-like heat-transport behaviors in the lattice. Depending on the vibration modes, phonons are classified as either acoustic or optical. Acoustic phonons represent the in-phase movements of all atoms in the lattice and generally have low frequencies as well as high group velocities and long mean free paths. Optical phonons at higher frequencies represent the out-of-phase movements of different atoms in the lattice and tend to possess low group velocities and short mean free paths. The lattice thermal conductivity in solids can be studied using kinetic theory [6], with $\kappa_L = 1/3C_Vvl$, where C_V is the heat capacity, v is the phonon group velocity, and l is the phonon mean free path. Because acoustic phonons usually have significantly higher v and longer l than optical phonons, they are typically considered the dominant contributors to the lattice thermal conductivity, and the role of optical phonons is far less studied in most materials. However, a recent study of SnS revealed that acoustic phonons are not the only source of κ_L, and more than 70% of the κ_L of SnS are actually contributed by its optical phonons [7]. Here, κ_L can be divided into the acoustic-phonon part κ_{La} and the optical-phonon part κ_{Lo}. In addition, κ_{Lo} has also been reported to account for over 20% of the κ_L in PbSe [8], PbTe [8], and $CoSb_3$ [9]. On the other hand, in some highly anharmonic crystals, heat is transported by the coupling of vibrational modes following the Allen–Feldman model [10]. This wave-like tunneling effect can be considered by calculating the off-diagonal elements of the heat-flux operators. A unified theory of both thermal transport mechanisms (*i.e.*, particle-like propagation and wave-like tunneling) has been successfully applied in calculations of the κ_L in $CsPbBr_3$ [11] and Si [12].

Recently, we found a rarely reported SnS-based material, $BaSnS_2$ [13], possessing nearly the same Sn–S skeleton with SnS, but with the additional heavy element Ba. More importantly, we found the optical phonons are also predominant in the heat transport in $BaSnS_2$, *i.e.*, over 68% of κ_L

contributed by its optical phonons, similar with that of 71% in SnS. Considering the similar Sn–S framework and the predominant optical phonon thermal conductivity in $BaSnS_2$ and SnS, it inspired our interest to study the correlation between the Sn–S framework and the optical phonon thermal conductivity in these materials.

In this work, we report the optical-phonon-dominated κ_L of $BaSnS_2$ and the underlying microscopic mechanism. The low diagonal lattice thermal conductivity κ_L(D) of $BaSnS_2$ was initially calculated using density functional theory (DFT) combined with Peierls–Boltzmann transport equation (PBTE) [14]. Further calculation based on Allen and Feldman model indicates that the off-diagonal components in heat flux operators also have moderate contributions to κ_L, which we define as κ_L(OD). The κ_L(OD) becomes pronounced at high temperatures and eventually leads to a deviation of the temperature dependence of κ_L from T^{-1} to $T^{-0.76}$, suggesting the potential lattice anharmonicity in $BaSnS_2$. We then calculated the mode-specific κ_L contribution to identify the κ_L-dominant phonons. The result suggests that optical phonons with relatively high group velocities dominate the κ_L. By visualizing the corresponding vibration modes, we attribute these relatively high-velocity optical phonons to the anti-phase vibrations in $BaSnS_2$ monolayers, which results from the unique permutation of SnS_3 tetrahedrons. Finally, through investigating the mode-resolved group velocity, relaxation time, and Grüneisen parameter, we ascribe the intrinsic low κ_L in $BaSnS_2$ to the soft lattice and the relatively high lattice anharmonicity resulting from the Ba–S weak bonding and Sn(II) lone pair electrons.

II. CALCULATION METHODS

All the DFT calculations were performed using the Vienna Ab initio Simulation Package (VASP) [15] implemented with the projector augmented wave (PAW) method [16]. We used a high plane-wave cutoff energy of 500 eV, with Ba 5*s*5*p*6*s* electrons, Sn 4*d*5*s*5*p* electrons, and S 3*s*3*p* electrons as valence electrons. The local density approximation (LDA) [17], Perdew–Burke–Ernzerhof (PBE) generalized gradient approximation (GGA) [18] and revised PBE-GGA for solids (PBEsol) [19] were all evaluated as the exchange-correlation functional. The comparison of the theoretical and experimental results [13,20–23] in Table 1 suggests that the LDA (or PBE) functional tends to underestimate (or overestimate) the lattice constants because of their well-known deficiency of over binding (or under binding) the chemical bonding. In contrast, the revised PBEsol-GGA functional overcomes this problem and yields the closest lattice parameters to the experimental values. Therefore, we adopted the PBEsol-GGA functional to relax the crystal structure of SnS and $BaSnS_2$, and then used it in the following self-consistent calculations. *k*-grids of 5 × 13 × 12 and 8 × 4 × 8 were applied for SnS and $BaSnS_2$ structure relaxation, respectively. The convergence criterion energy of the self-consistent step was 10^{-8} eV. The lattice parameters and atomic positions were fully relaxed until the Hellmann–Feynman forces between any two atoms were less than 10^{-3} eV Å^{-1}.

The lattice thermal conductivity κ_L can be obtained from Peierls–Boltzmann equation [24] as

$$\kappa_{\mathrm{L}} = \frac{\hbar^2}{V_{\mathrm{prim}} N k_{\mathrm{B}} T^2} \sum_{\mathbf{q}n} n_{\mathbf{q}n} \left[n_{\mathbf{q}n} + 1 \right] \omega_{\mathbf{q}n}^2 \mathbf{v}_{\mathbf{q}n} \otimes \mathbf{v}_{\mathbf{q}n} \tau_{\mathbf{q}n}, \tag{1}$$

where $\hbar$, V_{prim}, N, k_B, and T are, respectively, the reduced Planck constant, volume of the primitive cell, the number of sampled *q*-points, Boltzmann constant, and the absolute temperature. $\mathbf{q}$ and n index the wave vector and phonon branch of the phonon mode. n, ω, and $\mathbf{v}$, are, respectively, the Bose–Einstein distribution function, frequency, and group velocity of the corresponding phonon mode. We used Phonopy [25], a package implemented with the finite displacement method (FDM), to calculate the phonon dispersion and extract second-order interaction force constants (2nd-order IFCs), which is used to construct the dynamical matrix and calculate the harmonic phonon properties we mentioned above. To calculate the relaxation time τ, the anharmonic interaction must be considered. we employed the script thirdorder.py [14] to build the supercell configuration and extract third-order interaction force constants (3rd-order IFCs) to account for three-phonon scattering process. When generating the 2nd-order IFCs, we confirmed that a 3 × 3 × 3 supercell configuration for both SnS and $BaSnS_2$ was sufficient to cover all the long-range corrections. When generating the 3rd-order IFCs, a 2 × 4 × 4 supercell configuration and a 2 × 1 × 2 supercell configuration were built for SnS and $BaSnS_2$, respectively. After the interaction-force convergence test, we used a strict force cutoff radius of 0.5 nm for both compounds. Interactions between atoms spaced further than this radius were neglected and were considered as not contributing to the κ_L. Finally, the κ_L from diagonal terms of the heat-flux operators was calculated by finding the full iterative solution to the PBTE using ShengBTE [14] package. The κ_L contribution from off-diagonal terms of the heat-flux operators was calculated following the unified theory proposed by Simoncelli *et al*. [11] based on the single mode relaxation time approximation (SMRTA), which has been implemented and detailed in our earlier publications [26,27]

III. Results and Discussion

A. Crystal structure

As portrayed in Figure 1a, $BaSnS_2$ crystallizes in a layered monoclinic structure (space group $P2_1/c$, a = 6.08 Å, b = 12.14 Å, c = 6.24 Å) and shares similar structural features with SnS (space group *Pnma*, a = 11.18 Å, b = 3.98 Å, c = 4.33 Å) shown in Figure 1b. The in-plane directions of $BaSnS_2$ can be viewed as accordion-like Sn–S chains with minor distortions expanding along the c-axis. Ba^{2+} ions fill the interval between neighboring Sn–S chains along the a-axis. For the out-of-plane direction (the c-axis), except for the weak bonding between Sn–S layers, there is also weak ionic bonding between Ba^{2+} and S^{2-} from different layers of $BaSnS_2$. In SnS, the Sn(II) atom is in an asymmetric octahedral site. Instead of being in the octahedron center, it shifts closer to one of the triangular faces and coordinates with three S atoms via two short Sn–S bonds (2.57 Å) and one long Sn–S bond (2.60 Å), which permits the formation of a $5s^2$ lone pair [28,29] that occupies one corner of the SnS_3 tetrahedron, as shown in Figure S1a [30]. The neighboring corner-shared SnS_3 tetrahedrons tend to choose as-distant-as-possible positions to accommodate their lone pairs because of the electrostatic repulsion, while the symmetry guarantees that every two neighboring SnS_3 tetrahedrons can still coincide completely by rotating one of them towards the other. This unique zig-zag accordion-like shape of Sn–S chains are inherited by $BaSnS_2$, as illustrated in Figure S1b [30], with minor distortions in bond lengths (three Sn–S bonds at the length of 2.538, 2.598, and 2.615 Å) and bond angles. The further distortions of SnS_3 tetrahedrons in $BaSnS_2$ are due to the disturbance from weak bonding between Ba and S. In $BaSnS_2$, Ba^{2+} ions have distorted six-fold coordination with six S atoms from the neighboring Sn–S chains, with Ba–S bond lengths ranging from 3.12 to 3.19 Å. Such distorted structures in SnS and $BaSnS_2$ not only strengthen the lattice anharmonicity but also have a decisive influence on the prevalent vibration modes in the systems, which we will explain in detail in the vibration mode visualization section. In addition, we extracted the second-order interatomic force constant (2nd-order IFC) of $BaSnS_2$ and used it as an indicator for the bonding strength between the nearest neighbor pairs, as shown in Figure 1c. The higher 2nd-order IFC a nearest neighbor pair has, the stronger bonding it presents. As the covalent bonding skeleton of the system, the Sn–S bonding is undoubtedly the strongest, with the 2nd-order IFC of 8.67 eV/ Å^2. The Ba–S bonding, in contrast, is significantly weaker, with the 2nd-order IFC of only 2.71 eV/ Å^2. The weak bonding between Ba^{2+} ions and the Sn–S framework would significantly soften the lattice and slow down the phonon transport. The 2nd-order IFC of S–S interaction is 0.73 eV/ Å^2, indicating weak interlayer forces between Sn–S layers.

B. Phonon dispersion

The phonon dispersion and projected DOS for $BaSnS_2$ are presented in Figure 2. In $BaSnS_2$, most of the phonon bands are much flatter than those in SnS as shown in Figure S2 [30]. As the group velocity of phonon modes is the derivative of the phonon frequency with respect to the wave vector, this result suggests that phonon modes in $BaSnS_2$ have overall low group velocity, which we attribute to the weak bonding induced by Ba^{2+} ions. Meanwhile, several optical phonon branches in the range of 45–125 cm^{-1} and 200–275 cm^{-1} (in red windows in Figure 2) exhibit larger slopes than acoustic phonon branches, indicating relatively higher group velocities. This phenomenon is fairly uncommon as the group velocities of optical phonons in most materials tends to be much lower than acoustic phonons. These high-velocity optical phonons are related to anomalous high κ_{Lo} in $BaSnS_2$ according to our following analyses. On the other hand, all the optical phonon branches in Figure 2 are closely spaced to each other. When their frequency differences are smaller than their linewidths, there is a high chance these phonon modes will couple with each other and contribute to a wave-like tunneling transport. [11] This feature suggests that extra κ_L might exist if we take into account these wave-like tunneling phonons when calculating the κ_L of $BaSnS_2$. From projected DOS, we can tell that acoustic phonons and low-frequency optical phonons are mainly contributed by Ba^{2+} ions and Sn atoms, while the high-frequency optical phonons are dominated by the vibrations of S atoms.

C. Lattice thermal conductivity

Figure 3a displays the anisotropic κ_L(D) of $BaSnS_2$ and SnS along the *a*, *b*, and *c*-axis calculated by solving the PBTE [14]. The calculated room-temperature κ_L(D) of SnS along *a*, *b*, and *c* are 1.0, 2.9, and 2.1 W m^{-1} K^{-1}, which are close to the experimental results of He *et al.* [31]. $BaSnS_2$ exhibits a lower κ_L(D) than SnS in the corresponding directions. Especially along the *b*-axis (the out-of-plane direction), $BaSnS_2$ has a low κ_L(D) of merely 0.41 W m^{-1} K^{-1} at 300 K and eventually 0.15 W m^{-1} K^{-1} at 850 K. We also plotted the average κ_L(D) of $BaSnS_2$ by calculating the arithmetic average of κ_L(D) along three axes, which goes from 0.94 W m^{-1} K^{-1} at 300 K to 0.34 W m^{-1} K^{-1} at 850 K. In contrast, SnS has the average κ_L(D) of 2.03 W m^{-1} K^{-1} at 300 K and 0.73 W m^{-1} K^{-1} at 850 K. This result implies that weak bonding and structural distortions induced by Ba^{2+} ions might suppress the heat transport in the Sn–S framework. Recent studies [11,12,27,32] have clarified the importance of off-diagonal components in heat flux operators. Our phonon dispersion analysis also suggests the possible κ_L contributed by optical phonons with small frequency differences. Consequently, we calculated the off-diagonal lattice thermal conductivity κ_L(OD) separately to evaluate their contribution to the κ_L. Here, we define $\kappa_L = \kappa_L(\mathrm{D}) + \kappa_L(\mathrm{OD})$. As shown in Figure 3b, the κ_L(OD) has a different anisotropy with κ_L(D), *i.e.*, $\kappa_L^{b-\mathrm{axis}}(\mathrm{OD}) > \kappa_L^{c-\mathrm{axis}}(\mathrm{OD}) > \kappa_L^{a-\mathrm{axis}}(\mathrm{OD})$ .The $\kappa_L^{b-\mathrm{axis}}(\mathrm{OD})$ descends with the increasing temperature, while $\kappa_L^{a-\mathrm{axis}}(\mathrm{OD})$ and $\kappa_L^{c-\mathrm{axis}}(\mathrm{OD})$ ascend with the temperature. The total change of average κ_L(OD) with the temperature is less than 0.02 W m^{-1} K^{-1}, suggesting a weak temperature-dependence. The $\kappa_L^{a-\mathrm{axis}}(\mathrm{OD})$ and $\kappa_L^{c-\mathrm{axis}}(\mathrm{OD})$ at room temperature are negligible because they account for merely 10% of the κ_L along the corresponding direction. In comparison, $\kappa_L^{b-\mathrm{axis}}(\mathrm{OD})$ accounts for 35% of κ_L along the *b*-axis. This is consistent with the phonon dispersion in Figure 2, where the Γ-Z direction (corresponding to the *b*-axis) presents flatter and denser optical phonon branches than the other two directions. With the temperature T increasing, the κ_L(D) decreases following a T^{-1} manner, which makes the weakly temperature-dependent κ_L(OD) gradually comparable to κ_L(D) at high temperatures. Eventually, the $\kappa_L^{a-\mathrm{axis}}(\mathrm{OD})$ and $\kappa_L^{c-\mathrm{axis}}(\mathrm{OD})$ reach 23% and 31% of the κ_L along the corresponding directions, and $\kappa_L^{b-\mathrm{axis}}(\mathrm{OD})$ even reaches 56% of the κ_L along the *b*-axis. The gradually increasing average κ_L(OD) eases the decay of κ_L from T^{-1} to $T^{-0.76}$. Such deviation in the temperature-dependence of κ_L is also found in some highly anharmonic systems such as $Cu_{12}Sb_4S_{13}$ [27] and $TlInTe_2$ [32], suggesting the potential lattice anharmonicity in $BaSnS_2$. Compared to SnS (κ_L(OD) plotted in Figure S3 [30]), $BaSnS_2$ has a higher proportion of κ_L contributed by off-diagonal components because of the stronger coupling between closely spaced phonon modes suggested by its denser phonon dispersion. Furthermore, the weak bonding between Ba and S results in a generally lower group velocity of both diagonal and off-diagonal operators, thus leading to the lower κ_L as plotted in Figure 3c.

In the phonon gas model, each phonon mode contributes to κ_L(D) independently. In Allen–Feldman model, however, as the wave-like tunneling effect is always concerning two coupling phonons, it is inappropriate to attribute the κ_L contribution from this effect to a single phonon mode with a specific frequency and mean free path. Therefore, in the following κ_L contribution analyses, we discuss the κ_L-contribution from κ_L(OD) and κ_L(D) separately. In Figure 4a, we plot the two-mode-dependent contributions to average κ_L(OD) versus coupling phonon frequencies ω_1 and ω_2 at 300 K. This plot shows how much κ_L(OD) is contributed by two coupling phonons with frequency ω_1 and ω_2. The peaks mainly emerge around the diagonal ($\omega_1 = \omega_2$) in the frequency ranges of 45–125 cm^{-1} and 200–275 cm^{-1}, indicating the κ_L(OD) is mainly derived from the coupling of phonons with close frequencies. As we have observed in the phonon dispersion of $BaSnS_2$ that optical phonons in these frequency ranges tend to be more dispersive, the plot also suggests that optical phonons with relatively high group velocities dominate the κ_L(OD). We further calculated the contributions to κ_L(D) from three acoustic branches (the first transverse acoustic branch TA, the second transverse acoustic branch TA’, and the longitudinal acoustic branch LA) and all the optical branches with respect to the temperature. As observed in Figure 4b, in $BaSnS_2$, all the contributions to κ_L(D) tend to decrease with increasing temperature because of the strengthening of Umklapp scattering, whereas κ_{Lo}(D)/κ_L(D) maintains approximately 68%, similar to that 71% in SnS (demonstrated in Figure S4a [30]). Given that we already concluded κ_L(OD) is mainly derived from the coupling of two optical phonons with similar frequencies, the results in Figure 4a and 4b suggest the optical phonons have an even larger contribution to κ_L (over 68%) because they predominate in both κ_L(OD) and κ_L(D). To further investigate which part of optical phonons has a major contribution to the κ_L(D), we calculated the frequency dependence of the cumulative κ_L(D) at room temperature, as shown in Figure 4c. The cumulative κ_L(D) increases with the increasing frequency, for κ_L(D) contributions from phonons at different frequencies gradually add up. The cumulative κ_L(D) along three directions increase significantly in the frequency range 0–45 cm^{-1}, 45–125 cm^{-1}, and 200–275 cm^{-1}. The 0–45 cm^{-1} frequency range is populated mainly by acoustic phonons, while the other two frequency ranges corresponding to the relatively high-group-velocity optical phonons. Now we find that optical phonons falling in these ranges lead to the high κ_{Lo}(D) and κ_{Lo}(OD) simultaneously, which deserves to be further analyzed. In addition, we also plotted the normalized κ_L(D) integration versus phonon mean free path at 300 K in Figure 4d. The results indicate that 50% of κ_L(D) of $BaSnS_2$ is contributed by phonons with mean free paths shorter than 7.0 nm. This value further decreases to 2.4 nm at 850 K. Similar results for SnS are exhibited in Figure S4c [30]. Phonons with such small mean free paths can hardly be scattered by tens-of-nanometer-scale impurity centers or grain boundaries introduced by nanostructuring. Therefore, this method is expected to have a limited effect on the κ_L of $BaSnS_2$ and SnS, while alloying might be effective to modify these short-mean-free-path optical phonons, as He *et al.* [33] has succeeded in suppressing the κ_L of SnS by alloying it with Se.

D. Visualization of high-κ_L-contribution optical phonon modes

To specifically locate the most κ_L-contributive optical phonon modes, we calculated the κ_L(D) differential with respect to the phonon frequency. Obviously, with 32% of the κ_L(D) in $BaSnS_2$ contributed by only three acoustic branches within a narrow frequency range (0–45 cm^{-1}), the largest κ_L(D) differential should lie in the acoustic-phonon frequency range. However, because the total κ_L(D) contribution from optical phonons is larger than that from acoustic phonons, we focus only on the optical-phonon frequency range. As shown in Figure 5a, some low-frequency (45–125 cm^{-1}) optical phonons contribute significantly to the κ_L(D). We can then visualize the vibration modes belonging to this range and select one of them with the highest peak at ~50 cm^{-1} (VM1) as a representative. In the same way, we choose VM2 and VM3 in the frequency range 200–275 cm^{-1} to represent the vibration modes of high-frequency optical phonons. All the graphics of vibration mode visualization are made by VESTA 3 [34].

In Figure 5b–5d, we define the Ba–Sn–S layers stacking along the *b*-axis as sub-layer I–IV. The sub-layers I and II, as well as sub-layers III and IV, belong to the same $BaSnS_2$ monolayer. Atoms in each sub-layer have identical vibration amplitude but opposite vibration directions, which we call the anti-phase vibrations. For instance, in Figure 5b, all the atoms in sub-layer I vibrate mainly towards the positive *c*-axis, while in the neighboring sub-layer II all the atoms vibrate mainly towards the negative *c*-axis with the same amplitude. For the modes VM2 at ~200 cm^{-1} and VM3 at ~275 cm^{-1}, where S vibrations dominate, S atoms in the neighboring sub-layers also have similar anti-phase vibrations. As shown in Figure 5c, S atoms in sub-layers I and IV vibrate mainly towards the positive *c*-axis, whereas S atoms in sub-layers II and III vibrate towards the negative *c*-axis. In Figure 5d, S atoms present incomplete anti-phase movements. They all have partial eigenvectors towards the negative *b*-axis but combined with opposite partial eigenvectors along the *c*-axis. It is worth noting that owing to the influence of Ba^{2+} ions, S atoms between Ba^{2+} ions might have different vibrations with other S atoms that are exactly on the Sn–S chains, but they still present anti-phase vibrations in each sub-layer. The patterns of anti-phase vibrations can be observed more intuitively in SnS, where there is only pristine Sn–S framework without the interference of Ba^{2+} ions, as exhibited in Figure S5 [30]. These anti-phase vibrations are derived from the unique permutation of $\mathrm{SnS_3}$ tetrahedrons. As demonstrated in the crystal structure section, all the corner-shared neighboring $\mathrm{SnS_3}$ tetrahedrons have to accommodate the lone pairs at distant corners to diminish the electrostatic repulsion maximally. Consequently, the orientations of each neighboring $\mathrm{SnS_3}$ tetrahedrons are different with each other, but they can coincide with each other with certain rotating operations, as displayed in Figure 5b–5d. This unique symmetry combined with strong covalent Sn–S bonding inherited from SnS gives rise to highly synchronous anti-phase movements in $\mathrm{BaSnS_2}$. We rarely see Sn and S in the same sub-layer moving towards different directions even in other vibration modes that do not have as large κ_L-contributions as VM1, VM2, and VM3. This special anti-phase movement is similar to the famous pnicogen ring movement which is also corresponding to the heat-carrying optical phonon modes that account for 20% of the κ_L in skutterudite $\mathrm{CoSb_3}$ [9,35,36]. The former is the synchronous movement of the entire Sn–S chain, and the latter is the synchronous movement of the local $\mathrm{Sb_4}$ pnicogen ring. In Supplementary Information Sec. E [30], we demonstrate that three of the major heat-carrying optical modes in SnS also show these similar anti-phase movements. All these high-κ_L-contribution modes in $\mathrm{BaSnS_2}$ and SnS fall into the previously mentioned frequency ranges that relatively high-velocity optical phonon belongs to. They are supposed to be the representatives of the prevail vibration patterns in these high-velocity optical modes. In general, we visualized the vibration modes of optical phonons with the highest κ_L-contributions in $BaSnS_2$. They are highly synchronous anti-phase movements in $BaSnS_2$ monolayer, which is attributed to the unique permutation of SnS_3 tetrahedrons.

E. Mode-dependent group velocity, relaxation time, and Grüneisen parameters

To further investigate the properties of heat-carrying phonons, we quantitatively characterized all the phonon modes in $BaSnS_2$ by giving the mode-resolved group velocity v, relaxation time τ, and Grüneisen parameter γ from all the q-points in the irreducible Brillouin zone at room temperature. We also calculated the same parameters of SnS as references in Figure S6 [30]. As shown in Figure 6a, most of the phonon modes in $BaSnS_2$ present low group velocities less than 1 km s^{-1}. The overall low group velocity in $BaSnS_2$ is consistent with the flat phonon bands observed in Figure 2. Besides, the group velocities of optical phonons around 50 cm^{-1} are very close to that of the acoustic phonons, and some optical phonons around 275 cm^{-1} even possess higher group velocities than the acoustic ones, with a peak value of 4.7 km s^{-1} at 270 cm^{-1}. As we have mentioned above, these relatively high-velocity optical modes have high-κ_L-contribution and correspond to those anti-phase vibrations in $BaSnS_2$ monolayers. To give a more general description of the overall group velocity in $BaSnS_2$, we defined the mode average group velocity as

$$\bar{v} = \sqrt{\frac{\sum_{\mathbf{q}n} C_{\mathrm{V}\mathbf{q}n} v_{\mathbf{q}n}^2 \tau_{\mathbf{q}n} N_{\mathbf{q}n}}{\sum_{\mathbf{q}n} C_{\mathrm{V}\mathbf{q}n} \tau_{\mathbf{q}n} N_{\mathbf{q}n}}}, \tag{2}$$

where C_v, v, τ, and N are, respectively, the mode heat capacity, group velocity scalar, relaxation time, and symmetry degeneracy of corresponding mode $\mathbf{q}n$. This parameter reflects the general level of all the phonon modes over the entire Brillouin zone. We calculated $\bar{v}$ in $BaSnS_2$ to be 0.8 km s^{-1}. Compared to $\bar{v}$ of 1.1 km s^{-1} in SnS, lower mode average group velocity in $BaSnS_2$ confirms the lattice softening induced by Ba–S weak bonding.

Figure 6b shows the mode-resolved relaxation time (the reciprocal of phonon linewidths) with respect to the frequency. In $BaSnS_2$, acoustic phonons have relaxation time ranging from 1 to 100 ps, while most optical phonons have short relaxation times less than 10 ps, which indicates optical phonons have larger phonon linewidths than acoustic ones. These highly broadening and closely spaced optical phonon modes couple with each other easily and contribute to a substantial wave-like tunneling heat transport, which explains the origin of κ_{L}(OD) in $BaSnS_2$. The mode average relaxation time reads

$$\bar{\tau} = \frac{\sum_{\mathbf{q}n} C_{\mathrm{V}\mathbf{q}n} v_{\mathbf{q}n}^2 \tau_{\mathbf{q}n}}{\sum_{\mathbf{q}n} C_{\mathrm{V}\mathbf{q}n} v_{\mathbf{q}n}^2}. \tag{3}$$

We obtained $\bar{\tau}$ of 2.37 ps and 3.79 ps in $BaSnS_2$ and SnS, respectively. The likewise low $\bar{\tau}$ in $BaSnS_2$ and SnS implies potential high lattice anharmonicity in both systems.

The lattice anharmonicity can be explicitly measured by mode Grüneisen parameters γ defined as $\gamma_{\mathbf{q}n} = -\partial \ln \omega_{\mathbf{q}n} / \partial \ln V$ [37]. The γ quantifies the change of phonon frequencies ω with respect to the change of unit cell volume V. Positive or negative values of γ indicate the phonon frequency softening or hardening with the expansion of lattice. Larger absolute values of γ indicate the higher lattice anharmonicity in compounds. Solids with weak anharmonicity usually present γ lower than 1, while those with strong anharmonicity have γ close to or higher than 1 [38], such as InTe ($\gamma \sim$ 1.00) [39], PbTe ($\gamma \sim$1.40) [40], and BiCuSeO ($\gamma \sim$1.50) [41]. From Figure S6c [30], we can tell that most heat-carrying phonons in SnS have γ larger than 1, especially those high-frequency optical phonons with γ ranging from 1 to 4. According to previous studies [28,42–44], the high lattice anharmonicity in SnS is originated from the lone pair electrons of Sn(II). $BaSnS_2$ inherits this feature (we have elaborated in the crystal structure section) and presents even stronger lattice anharmonicity due to the extra disturbance that Ba^{2+} ions bring to the Sn–S framework. As plotted in Figure 6c, phonon modes in the frequency range 0–125 cm^{-1} present high Grüneisen parameters ranging from −6 to +2, suggesting high anharmonicity of certain acoustic phonon modes and low-frequency optical phonon modes in $BaSnS_2$. The high-frequency optical phonon modes possess relatively lower Grüneisen parameters ranging from +1 to +2. We define the mode average Grüneisen parameters as

$$\bar{\gamma} = \frac{\sum_{\mathbf{q}n} \left|\gamma_{\mathbf{q}n}\right| C_{\mathrm{V}\mathbf{q}n}}{\sum_{\mathbf{q}n} C_{\mathrm{V}\mathbf{q}n}} \tag{4}$$

The $\bar{\gamma}$ of $BaSnS_2$ and SnS is 1.24 and 1.08, respectively, indicating overall higher lattice anharmonicity in $BaSnS_2$. Our calculated Grüneisen parameters are derived from three-phonon interaction, as the strong lattice anharmonicity of SnS is reported more often at high temperatures [45–47], we believe considering the phonon frequency shifting induced by higher order anharmonicity (such as quartic anharmonicity) at high temperature will offer a more comprehensive understanding of the lattice anharmonicity in both compounds. In Figure S7 [30], the potential energy surfaces (PES) were plotted and fitted with polynomials up to the second and fourth order, respectively, following the formalism proposed by Skelton *et al.* [48] The result shows PES of typical phonon modes in $BaSnS_2$ deviate more from the harmonic approximation than in SnS by considering up to quartic anharmonicity, implying potential higher lattice anharmonicity might be contributed from high-order anharmonic terms in $BaSnS_2$. We realized that by performing phonon renormalization with cubic and quartic anharmonicity, a more explicit relation between the lattice anharmonicity and thermal conductivity could be unveiled. However, recent studies [49–51] have demonstrated the complex interplay between phonon renormalization, four-phonon scattering, and thermal expansion. In our previous study [52], the opposite influence that phonon renormalization and four-phonon scattering might have on the κ_L makes it nontrivial to clarify the relation between high-order anharmonicity and κ_L. Given that $BaSnS_2$ has a large primitive cell (16 atoms), it requires tremendous resources and time to compute the four-phonon scattering rates and renormalize phonon frequencies with cubic and quartic anharmonicity. Therefore, it is practical to conclude with current results that $BaSnS_2$ has a stronger lattice anharmonicity than *Pnma* phase SnS whose low κ_L is previously attributed to the strong lattice anharmonicity [7,20].

In conclusion, the low group velocity, low relaxation time (large phonon linewidth), and high Grüneisen parameter indicate the soft and anharmonic lattice of $BaSnS_2$, which slows down the entire phonon transport process and leads to an intrinsic low κ_L.

IV. Conclusion

Using the DFT methods combined with Peierls–Boltzmann transport theory, we first calculated the diagonal lattice thermal conductivity κ_L(D) derived from particle-like phonon transport in $BaSnS_2$. The average κ_L(D) is less than half of that in SnS, with a low value of 0.34 W m^{-1} K^{-1} at 850 K. By taking into account the off-diagonal terms of general group velocity operates, we found additional off-diagonal lattice thermal conductivity κ_L(OD) contributed by wave-like tunneling phonon transport. With temperature increasing, the κ_L(OD) accounts for a higher proportion in κ_L and finally reaches 33% of the κ_L at 850 K. It leads to a milder decay of T-dependence of κ_L from T^{-1} to $T^{-0.76}$, indicating the potential lattice anharmonicity in $BaSnS_2$. Subsequent mode-specific κ_L-contribution investigations suggest that over 68% of κ_L in $BaSnS_2$ is contributed by optical phonons. This anomalous optical-phonon-dominated κ_L is ascribed to the relatively high group velocity of the heat-carrying optical phonons. These relatively high-velocity modes are then visualized as the anti-phase vibrations in $BaSnS_2$ monolayers, resulting from the unique permutation of SnS_3 tetrahedrons. Eventually, the low group velocity, low relaxation time, and high Grüneisen parameter are found in $BaSnS_2$, suggesting the soft lattice and relatively high lattice anharmonicity induced by Ba^{2+} ions and Sn(II) lone pair electrons. All these factors suppress the phonon transport and contribute to the intrinsic low κ_L. $BaSnS_2$ is a special compound that nearly inherits the entire Sn–S conductive network from SnS while presenting much lower κ_L. Recent progress in experimental studies of SnS-based thermoelectrics implies that $BaSnS_2$ might also be a potential candidate for high-performance thermoelectric materials. Our study reveals the microscopic mechanism of heat transport in $BaSnS_2$ and suggests it worthy of further experimental studies as an intrinsic-low-κ_L material.

Acknowledgment

This work at Northwestern University was supported by a grant from the U.S. Department of Energy, Office of Science, and Office of Basic Energy Sciences under award number DE-SC0014520. The Northwestern Quest computational resources are acknowledged. X.T. wishes to acknowledge support from the National Key Research and Development Program of China (2019YFA0704902), Natural Science Foundation of China (grant nos. 51972256, 51872219, 51632006, and 51521001), and 111 Project of China (grant no. B07040). Z.L. was supported by the China Scholarship Council (grant no. 201906950054) for a two-year study at Northwestern University.

References

[1] H. J. Goldsmid, *Introduction to Thermoelectricity*, Vol. 121 (Springer Berlin Heidelberg, Berlin, Heidelberg, 2016).

[2] R. Hanus, M. T. Agne, A. J. E. Rettie, Z. Chen, G. Tan, D. Y. Chung, M. G. Kanatzidis, Y. Pei, P. W. Voorhees, and G. J. Snyder, Adv. Mater. **31**, 1 (2019).

[3] G. Pernot, M. Stoffel, I. Savic, F. Pezzoli, P. Chen, G. Savelli, A. Jacquot, J. Schumann, U. Denker, I. Mönch, C. Deneke, O. G. Schmidt, J. M. Rampnoux, S. Wang, M. Plissonnier, A. Rastelli, S. Dilhaire, and N. Mingo, Nat. Mater. **9**, 491 (2010).

[4] A. Shakouri, Proc. IEEE **94**, 1613 (2006).

[5] D. R. Clarke and C. G. Levi, Annu. Rev. Mater. Res. **33**, 383 (2003).

[6] J. M. Ziman, *Electrons and Phonons: The Theory of Transport Phenomena in Solids* (Oxford University Press, Oxford, 2001).

[7] R. Guo, X. Wang, Y. Kuang, and B. Huang, Phys. Rev. B **92**, 115202 (2015).

[8] Z. Tian, J. Garg, K. Esfarjani, T. Shiga, J. Shiomi, and G. Chen, Phys. Rev. B **85**, 184303 (2012).

[9] R. Guo, X. Wang, and B. Huang, Sci. Rep. **5**, 1 (2015).

[10] I. Pallecchi, N. Manca, B. Patil, L. Pellegrino, and D. Marré, Nano Futur. **4**, 1 (2020).

[11] M. Simoncelli, N. Marzari, and F. Mauri, Nat. Phys. **15**, 809 (2019).

[12] L. Isaeva, G. Barbalinardo, D. Donadio, and S. Baroni, Nat. Commun. **10**, 1 (2019).

[13] J. E. Iglesias and H. Steinfink, Acta Crystallogr. Sect. B Struct. Crystallogr. Cryst. Chem. **29**, 1480 (1973).

[14] W. Li, J. Carrete, N. A. Katcho, and N. Mingo, Comput. Phys. Commun. **185**, 1747 (2014).

[15] G. Kresse and J. Furthmüller, Phys. Rev. B **54**, 11169 (1996).

[16] P. E. Blöchl, Phys. Rev. B **50**, 17953 (1994).

[17] J. P. Perdew and A. Zunger, Phys. Rev. B **23**, 5048 (1981).

[18] J. P. Perdew, K. Burke, and M. Ernzerhof, Phys. Rev. Lett. **77**, 3865 (1996).

[19] J. P. Perdew, A. Ruzsinszky, G. I. Csonka, O. A. Vydrov, G. E. Scuseria, L. A. Constantin, X. Zhou, and K. Burke, Phys. Rev. Lett. **100**, 1 (2008).

[20] S. Hao, V. P. Dravid, M. G. Kanatzidis, and C. Wolverton, APL Mater. **4**, (2016).

[21] R. Ibragimova, M. Ganchenkova, S. Karazhanov, and E. S. Marstein, Philos. Mag. **98**, 710 (2018).

[22] A. R. H. F. Ettema, R. A. De Groot, C. Haas, and T. S. Turner, Phys. Rev. B **46**, 7363 (1992).

[23] S. Del Bucchia, J. C. Jumas, and M. Maurin, Acta Crystallogr. Sect. B Struct. Crystallogr. Cryst. Chem. **37**, 1903 (1981).

[24] R. E. Peierls, *Quantum Theory of Solids* (Clarendon Press, 1996).

[25] A. Togo and I. Tanaka, Scr. Mater. **108**, 1 (2015).

[26] Y. Xia, V. I. Hegde, K. Pal, X. Hua, D. Gaines, S. Patel, J. He, M. Aykol, and C. Wolverton, Phys. Rev. X **10**, 41029 (2020).

[27] Y. Xia, V. Ozoliņš, and C. Wolverton, Phys. Rev. Lett. **125**, 43 (2020).

[28] A. Walsh, D. J. Payne, R. G. Egdell, and G. W. Watson, Chem. Soc. Rev. **40**, 4455 (2011).

[29] A. Walsh and G. W. Watson, 18868 (2005).

[30] See Supplementral Material at [URL] for partial charge density, phonon dispersion, κ_L(OD) of SnS, κ_L contribution in SnS, phonon mode visualization, mode-resolved parameters, and potential energy surfaces.

[31] W. He, D. Wang, J.-F. Dong, Y. Qiu, L. Fu, Y. Feng, Y. Hao, G. Wang, J. Wang, C. Liu, J.-F. Li, J. He, and L.-D. Zhao, J. Mater. Chem. A **6**, 10048 (2018).

[32] K. Pal, Y. Xia, and C. Wolverton, Npj Comput. Mater. **7**, (2021).

[33] W. He, D. Wang, and Haijun Wu, Science (80-.). **1424**, 1418 (2019).

[34] K. Momma and F. Izumi, J. Appl. Crystallogr. **44**, 1272 (2011).

[35] J. Feldman and D. Singh, Phys. Rev. B - Condens. Matter Mater. Phys. **53**, 6273 (1996).

[36] H. Chi, H. Kim, J. C. Thomas, X. Su, S. Stackhouse, M. Kaviany, A. Van der Ven, X. Tang, and C. Uher, Phys. Rev. B **86**, 195209 (2012).

[37] M. T. Dove and M. T. Dove, *Structure and Dynamics: An Atomic View of Materials*, Vol. 1 (Oxford University Press, 2003).

[38] E. S. Toberer, A. Zevalkink, and G. J. Snyder, J. Mater. Chem. **21**, 15843 (2011).

[39] D. P. Spitzer, J. Phys. Chem. Solids **31**, 19 (1970).

[40] D. T. Morelli, V. Jovovic, and J. P. Heremans, Phys. Rev. Lett. **101**, 16 (2008).

[41] Y. L. Pei, J. He, J. F. Li, Fuli, Q. Liu, W. Pan, C. Barreteau, D. Berardan, N. Dragoe, and L. D. Zhao, NPG Asia Mater. **5**, (2013).

[42] P. Wu, K. Xia, K. Peng, T. Honda, K. Ikeda, F. Liu, P. Vallobra, F. Fan, J. Song, D. Zhang, F. Yu, J. Ying, F. Zhu, T. Otomo, T. Kamiyama, and W. Zhao, Phys. Rev. B **103**, 1 (2021).

[43] N. Ouyang, C. Wang, Z. Zeng, and Y. Chen, Appl. Phys. Lett. **119**, (2021).

[44] M. K. Jana and K. Biswas, ACS Energy Lett. **3**, 1315 (2018).

[45] T. Chattopadhyay, J. Pannetier, and H. G. Von Schnering, J. Phys. Chem. Solids **47**, 879 (1986).

[46] U. Aseginolaza, R. Bianco, L. Monacelli, L. Paulatto, M. Calandra, F. Mauri, A. Bergara, and I. Errea, Phys. Rev. B **100**, 214307 (2019).

[47] T. Lanigan-Atkins, S. Yang, J. L. Niedziela, D. Bansal, A. F. May, A. A. Puretzky, J. Y. Y. Lin, D. M. Pajerowski, T. Hong, S. Chi, G. Ehlers, and O. Delaire, Nat. Commun. **11**, 1 (2020).

[48] J. M. Skelton, L. A. Burton, S. C. Parker, A. Walsh, C. E. Kim, A. Soon, J. Buckeridge, A. A. Sokol, C. R. A. Catlow, A. Togo, and I. Tanaka, Phys. Rev. Lett. **117**, 1 (2016).

[49] Y. Xia, Appl. Phys. Lett. **113**, (2018).

[50] N. K. Ravichandran and D. Broido, Phys. Rev. B **98**, 1 (2018).

[51] T. Feng, X. Yang, and X. Ruan, J. Appl. Phys. **124**, (2018).

[52] Y. Xia, V. I. Hegde, K. Pal, X. Hua, D. Gaines, S. Patel, J. He, M. Aykol, and C. Wolverton, Phys. Rev. X **10**, 1 (2020).

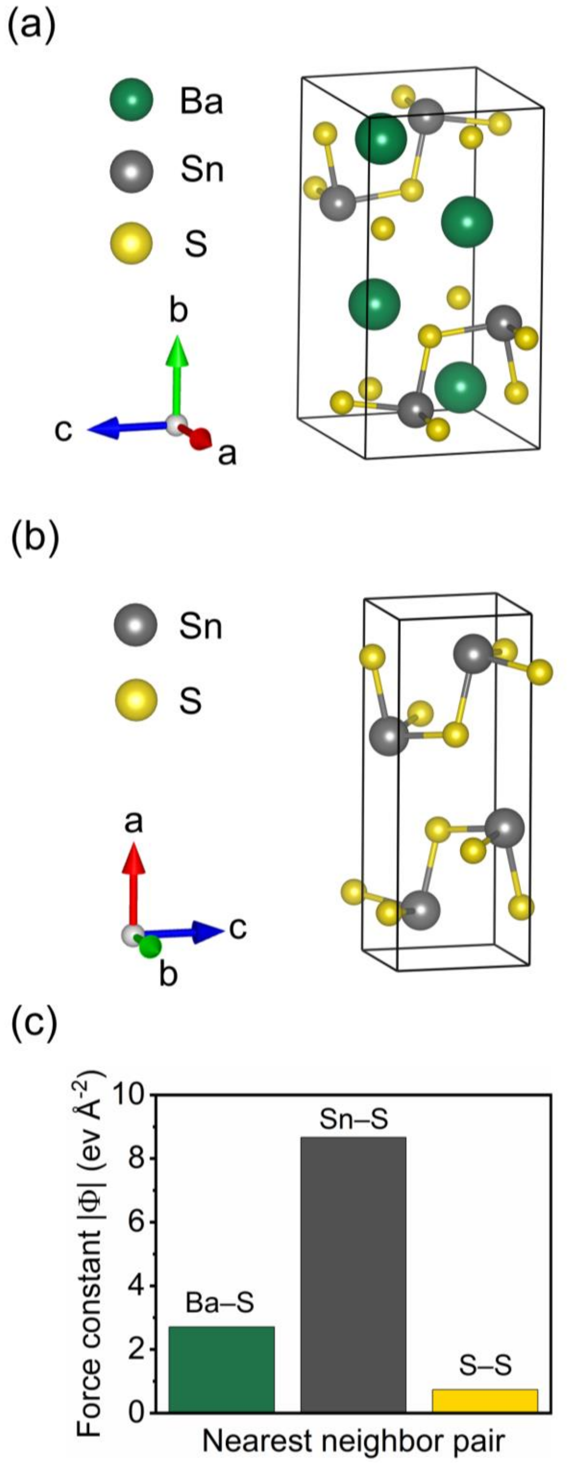

Figure 1. (a) The crystal structure of BaSnS$_2$. (b) The crystal structure of SnS. (c) The second-order interatomic force constants (2nd-order IFCs) of the nearest neighbor pairs in BaSnS$_2$. The 2nd-order IFC serves as an indicator for the bonding strength between the nearest neighbor pairs. The higher 2nd-order IFC a nearest neighbor pair has, the stronger bonding it presents.

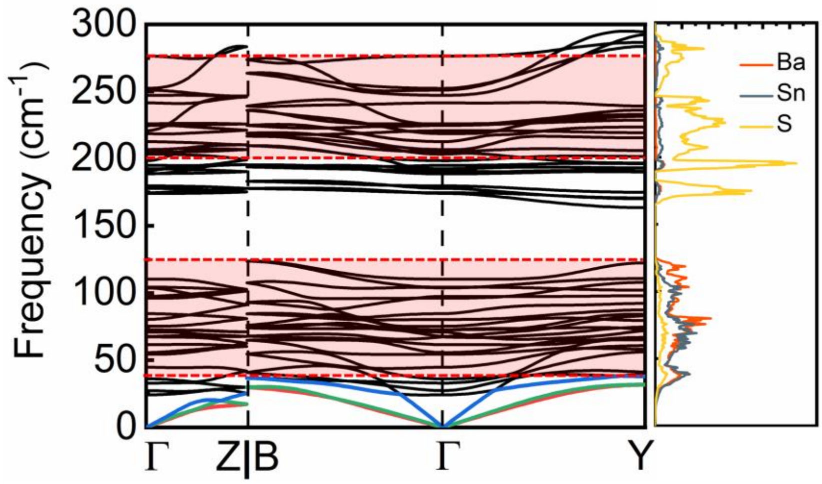

Figure 2. The phonon dispersion and projected density of states of $BaSnS_2$. The frequency ranges in red windows (45–125 cm^{-1} and 200–275 cm^{-1}) indicate optical phonons with group velocities close to or higher than acoustic phonons.

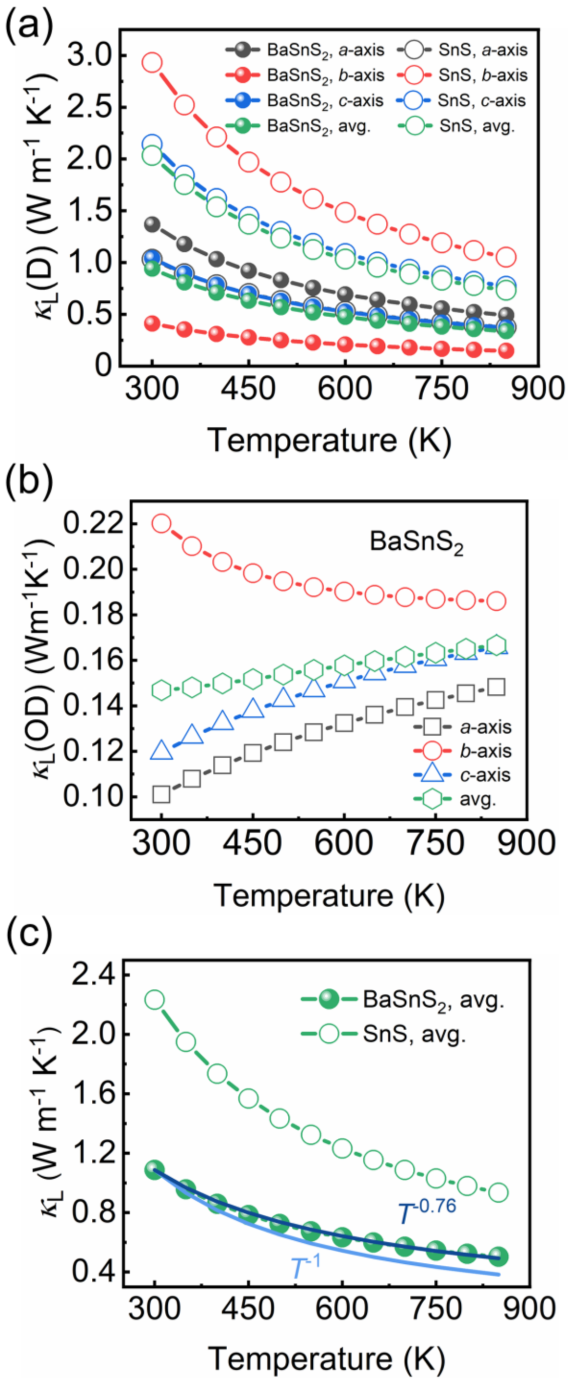

Figure 3. (a) The calculated diagonal lattice thermal conductivity κ_L(D) as a function of temperature in $BaSnS_2$ and SnS. (b) The calculated off-diagonal term lattice thermal conductivity κ_L(OD) as a function of temperature in $BaSnS_2$. (c) The calculated total lattice thermal conductivity $\kappa_L = \kappa_L(D) + \kappa_L(OD)$ as a function of temperature in $BaSnS_2$ and SnS. The solid lines without symbols are fitting lines indicating how κ_L decays with temperature T.

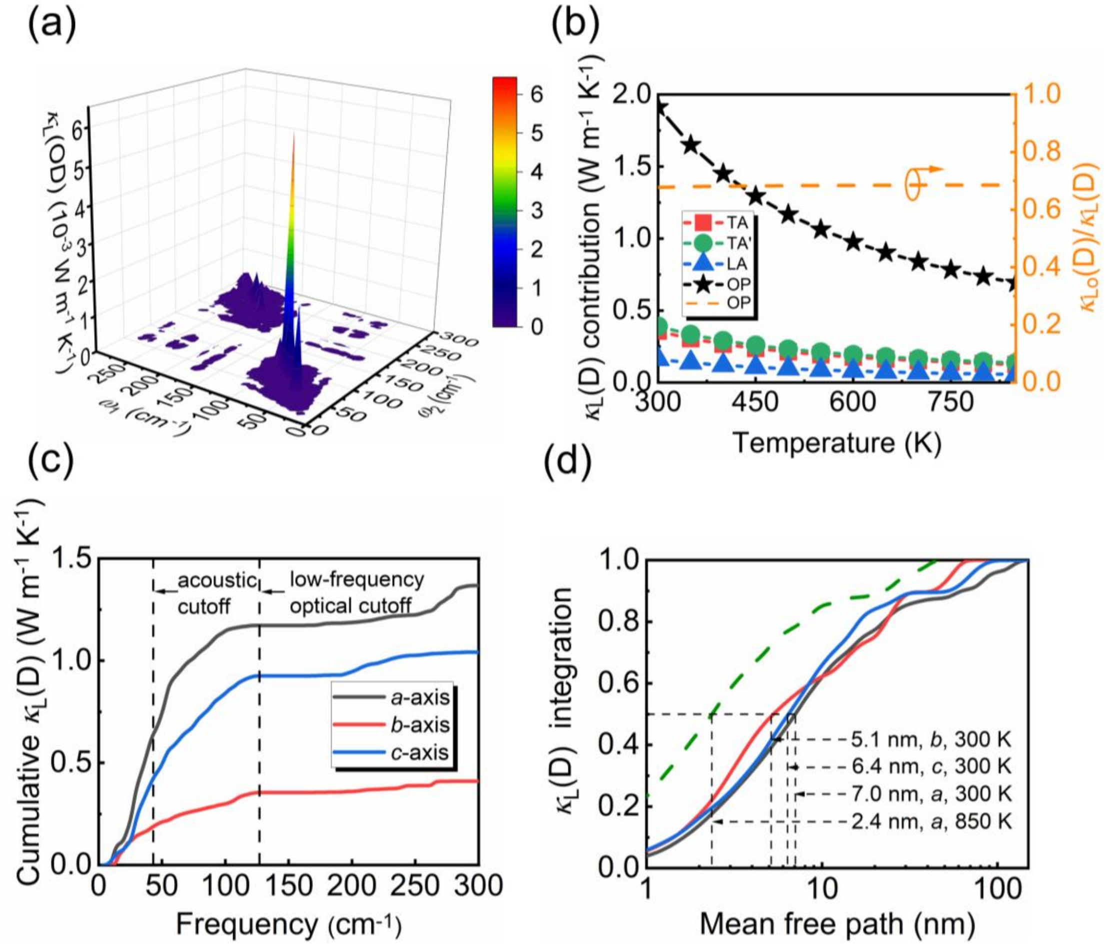

Figure 4. (a) The two-mode-dependent contributions to average κ_L(OD) versus coupling phonon frequencies ω_1 and ω_2 at 300 K. (b) The temperature dependence of κ_L(D) contribution from three acoustic phonon branches (TA, TA', and LA) and all the optical branches (OP) in $BaSnS_2$. Note that κ_L(D) here is the sum of diagonal lattice thermal conductivities along three axes. The right-hand axis indicates the ratio of optical-phonon-contributed lattice thermal conductivity κ_{Lo}(D) to the κ_L(D). (c) The frequency dependence of cumulative κ_L(D) at room temperature. (d) The mean free path dependence of κ_L(D) integration at 300 K and 850 K.

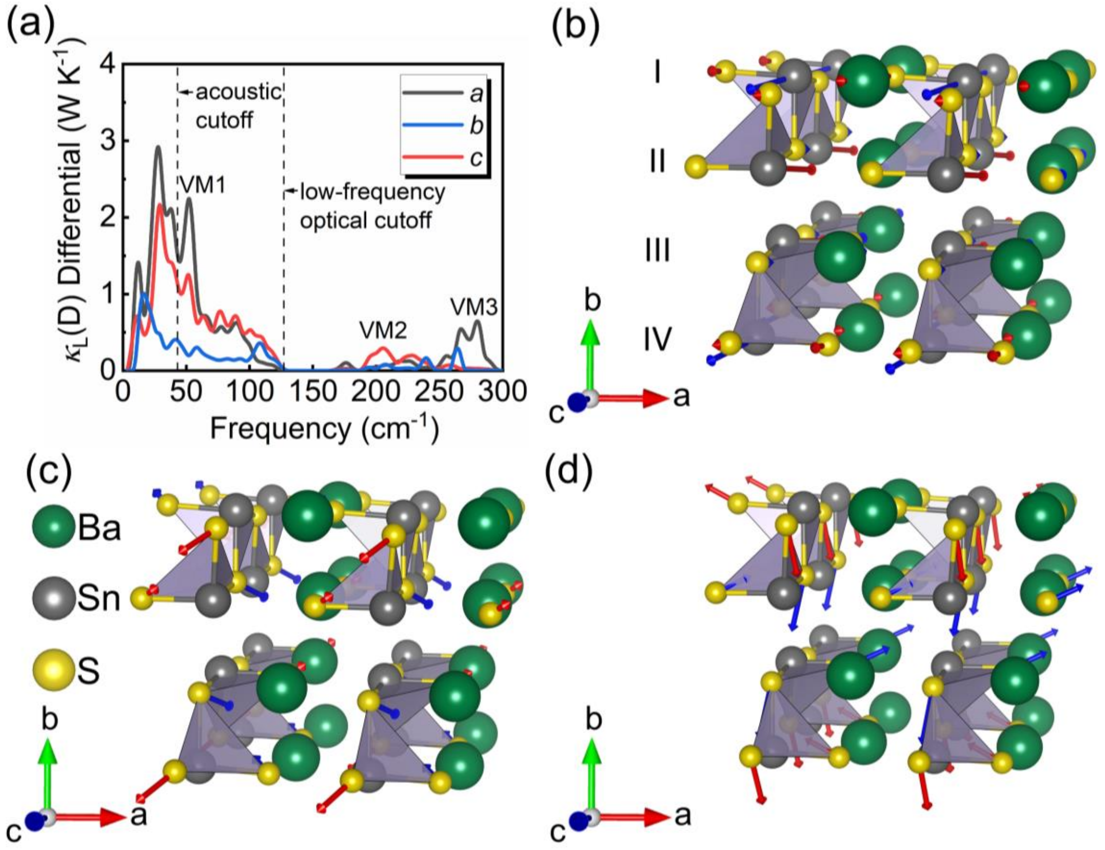

Figure 5. (a) The κ_L(D) differential with respect to phonon frequency in $BaSnS_2$. The peaks of the most κ_L-contributive vibration modes are marked as VM1 at ~50 cm^{-1}, VM2 at ~200 cm^{-1}, and VM3 at ~275 cm^{-1}. (b)–(c) The visualization of corresponding vibration modes. The 2 × 1 × 2 $BaSnS_2$ supercell is divided into I–IV sub-layers according to different orientations of SnS_3 tetrahedrons between neighboring sub-layers. The eigenvectors of vibrations are indicated by arrows. Arrows with different colors (blue and red) indicate pairs of anti-phase vibrations in each $BaSnS_2$ monolayer. The SnS_3 tetrahedrons are colored in gray to better indicate their different orientations in each sub-layer.

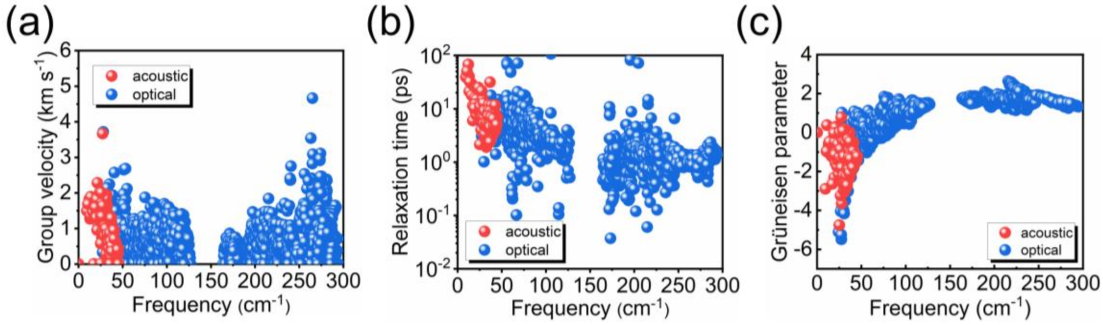

Figure 6. The mode-resolved (a) group velocity (b) relaxation time (c) Grüneisen parameter versus phonon frequency in $BaSnS_2$ at room temperature.

Table 1 The lattice parameters of SnS and $BaSnS_2$ from this work and literatures.

	SnS			$BaSnS_2$		
	a (Å)	*b* (Å)	*c* (Å)	*a* (Å)	*b* (Å)	*c* (Å)
PBEsol (this work)	11.09	3.99	4.23	6.06	12.11	6.23
PBE (this work)	11.43	4.02	4.45	6.19	12.54	6.35
LDA (this work)	10.97	3.95	4.19	6.00	11.91	6.16
PBE (Ref. 20)	11.42	4.02	4.46			
LDA (Ref. 21)	10.96	3.95	4.20			
Experiment (Ref. 22)	11.20	3.99	4.33			
Experiment (Ref. 23)	11.18	3.98	4.33			
Experiment (Ref. 13)				6.08	12.14	6.24